Eleventh International Conference on CFD in the Minerals and Process Industries
CSIRO, Melbourne, Australia
7-9 December 2015

DEVELOPMENT OF A SLURRY ABRASION MODEL USING AN EULERIAN-EULERIAN 'TWO-FLUID' APPROACH

Peter RIZKALLA[1] and David F. FLETCHER[2]

[1] LEAP Australia Pty Ltd, Bentley, WA 6102, AUSTRALIA
[2] School of Chemical and Biomolecular Engineering, University of Sydney, NSW 2006, AUSTRALIA

ABSTRACT

The aim of the present study was to develop a numerical model that predicts the quantity and location of erosion damage in slurry systems susceptible to erosive wear. Unlike many forms of erosion which often need to be prevented, hydro-erosion is deliberately introduced during the manufacturing process of automotive diesel injector nozzles to smoothen out imperfections in the spray-hole geometry. This model has been integrated into a commercial CFD code, ANSYS CFX®, and takes into account the change in geometry by dynamically updating the mesh to model the removal of material.

A slurry jet erosion apparatus was developed to determine experimentally the parameters influencing the erosion process. Simplified planar geometries with four different angles of inclination were investigated and subject to typical hydro-erosive conditions similar to that used during the smoothing process of injector spray-hole geometries. In addition, the effect of slurry viscosity, particle size and concentration were studied. Results were used to calibrate the developed erosion model which showed encouraging trends in comparison with experimental studies for predicting the location and quantity of erosive wear.

NOMENCLATURE

A_w	wall cell face area	W_e	work energy
C_a	abrasion constant	W_n	normal wear
d_p	particle diameter	W_t	tangential wear
E_k	kinetic energy	Δx	erosion length
F_n	normal force	Δy	erosion depth
F_t	tangential force	y^+	wall distance parameter
H_w	wall hardness		
k	turbulence kinetic energy	α_p	particle impact angle
		β	inclination angle
k_a	abrasion amplitude	γ_c	specific cutting energy
l_s	sliding length	ϕ_p	particle volume fraction
m	concentration index	φ_p	particle mass fraction
m_p	particle mass	η	wall normal distance
$\vec{n}$	normal vector	λ_p	particle shape factor
p	fluid pressure	μ	slurry mixture viscosity
P	probability function	μ_f	dynamic fluid viscosity
r_p	particle radius	ρ_f	fluid density
Re	Reynolds number	ρ_p	particle density
t	time	σ	standard deviation
U_n	normal velocity	τ_w	wall shear stress
U_p	particle velocity		
U_t	tangential velocity		
V	control volume		

INTRODUCTION

The hydro-erosion process has been successfully implemented as a crucial step in the manufacturing process of diesel injector nozzles. The process takes place by forcing an abrasive liquid-solid slurry mixture at high pressure through the injector spray holes which wears the material at the edges and surfaces resulting in an increased discharge coefficient and improvement in flow rate variability. The process must however be carefully controlled to avoid excessive wear rates which lead to an uncontrolled rate of wear accompanied by undesirable geometry configurations thus reducing the overall efficiency of the flow. Figure 1 below shows the effects of hydro-erosion as a function of time at different stages of the process.

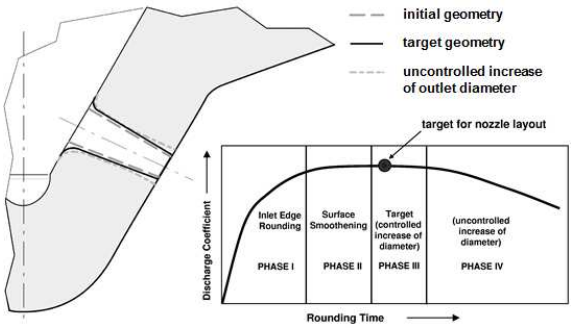

Figure 1: The hydro-erosion grinding process applied to a diesel injector nozzle.

Despite its success, the basic physical principles and core understanding of the process itself are not fully understood. In fact, for this reason the process has often been termed a 'black box' since a combination of input parameters results in a certain output without real insight into the erosion process. Therefore, being able to predict the quantity and location of the eroded material will lead to a better understanding of the complete process which in turn will lead to the potential for a reduction in manufacturing time and cost but ultimately improved engine performance and reduced emissions.

EXPERIMENTAL PROCEDURE

The erosion device used for the present study consisted of a closed-loop slurry circuit comprising of a 15 litre slurry tank, an aggregate and main pump responsible for delivering the slurry to the erosion specimen, and a testing head which carries the erosion specimen. A diagram showing the main components of the testing head are shown

in Figure 2. The specimen to be tested is placed between a pair of 60 mm diameter transparent windows to allow the flow to be visualised in real time by means of a light source and CCD camera facing each other and placed at either side of the testing head.

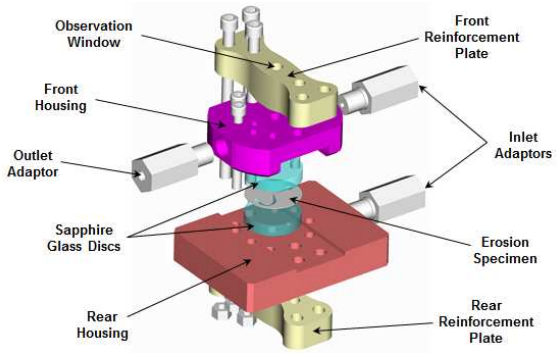

Figure 2: Exploded view of the erosion testing head.

The slurry mixture was transported to the specimen via two inlet ports normal to the test specimen and drained back to the tank via a single outlet port. Before reaching the specimen, the flow rate, density and temperature of the slurry were measured. Two opposing inlet ports were used to minimise effects of any asymmetry in the flow. Two pressure sensors located about 35 mm upstream and downstream of the observation windows measured the inlet and outlet pressures, respectively. Likewise, two thermocouples placed further upstream and downstream, measure the slurry temperature as it enters and exits the testing head. A ball valve installed downstream of the testing head was necessary to regulate the back-pressure in order to avoid the onset of cavitation.

The erosion specimens used for the present study were simplified planar geometries constructed from 1 mm thick sheets of chromium-nickel based stainless steel, similar to that used for diesel injector nozzles. An example of the specimen mounted in the testing head is shown below.

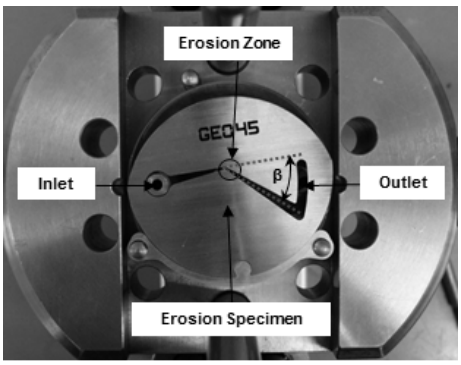

Figure 3: Photograph of erosion specimen mounted on testing head.

The profiles were laser cut for precision, and have the same underlying layout, namely, an inlet port to the left (where the slurry enters), followed by a converging-diverging section in the centre (where maximum velocity is attained and particle erosion takes place), and an outlet port on the right (where the slurry exits). The main difference in the geometries can be seen in the inclination angle (measured from the mean horizontal flow path) which was one of the parameters to be investigated in terms of its effect on the erosion rate (see Figure 3).

Parametric Study

A parametric study was conducted in order to investigate the primary effects of geometry inclination angle, fluid viscosity, particle concentration and particle size on the erosion rate. To understand the effect of each of these parameters, it was necessary to change only one variable at a time systematically, giving rise to the test matrix, as shown in Table 1, consisting of 20 tests in total. Each test was conducted twice to ensure repeatability.

Test No.	Inclination Angle (deg)				Fluid Viscosity (mPa·s)			Particle Size (μm)		Mass Fraction (%)	
	45	60	75	90	5	10	32	4.5	44.5	1	2
1	●					●		●		●	
2		●				●		●		●	
3			●			●		●		●	
4				●		●		●		●	
5	●				●			●		●	
6		●			●			●		●	
7			●		●			●		●	
8				●	●			●		●	
9	●						●	●		●	
10		●					●	●		●	
11			●				●	●		●	
12				●			●	●		●	
13	●					●		●			●
14		●				●		●			●
15			●			●		●			●
16				●		●		●			●
17	●					●			●	●	
18		●				●			●	●	
19			●			●			●	●	
20				●		●			●	●	

Table 1: Matrix of runs for parametric study.

The erosion specimen was weighed before and after each test to determine the amount of material removed. This process was repeated five times and an average value for the mass removal was recorded. Before this could be done, each specimen was cleaned in an ultrasonic water bath and dried with pressurised air to ensure they were completely free of any contamination. Although the mass removed does provide information about the erosion rate on a global scale and indeed the repeatability of each test, it does not provide any local information about the erosion profile nor its location. In light of this, the length and depth of the eroded surface was measured using laser topography, see typical case in Figure 4, and these were used to validate the developed erosion model.

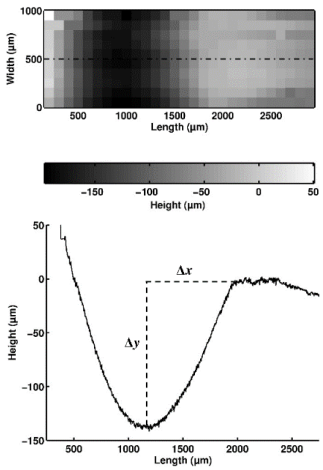

Figure 4: Erosion contour map measured for a selected sample using laser topography. (a) Surface plot and (b) centreline profile.

Effect of Fluid Viscosity and Inclination Angle

To investigate the effect of viscosity and the wall lubricating film, three different mineral oils were tested having relatively low, moderate and high viscosities, denoted by Oils 1-3, respectively. These are the same fluids used in the hydro-erosion of diesel injector nozzles. In order for the erosion quantities to be comparable, it was necessary to normalise the erosion quantities with respect to total exposure time and velocity squared. Results are presented below in Figure 5.

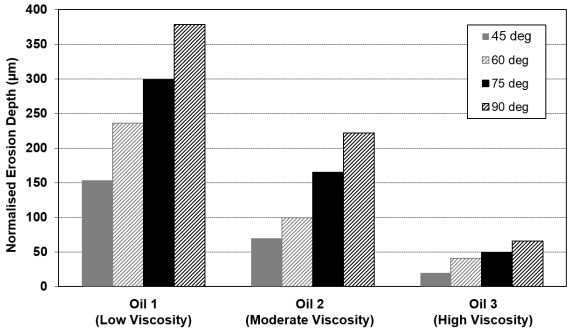

Figure 5: Effect of fluid viscosity on erosion depth for different inclination angles.

The erosion depth increases with decreasing viscosity and with increasing inclination angle. Furthermore, the variation is greater for lower fluid viscosities and is consistent with what is observed with the hydro-erosion of diesel injector nozzles. The effect of reduced viscosity can be explained by the higher Stokes number indicating a greater tendency for particles to deviate from the fluid streamlines and more easily penetrate the lubricating film. The runs with Oil 3 (highest viscosity and lowest bulk velocity) also exhibited a somewhat different erosion profile to those using Oils 1 and 2 as it appeared that surface smoothing had only taken place rather than actual wearing of the material possibly due to the lower Reynolds numbers, implying that the flow was laminar $(Re < 2{,}300)$ and therefore predominantly governed by fluid viscous forces, making it even more difficult for particles to penetrate the lubricating film.

The inclination angle was chosen as a variable to investigate since it is known that even slight changes in the intersection angles of injector spray holes can have a profound impact on the erosion pattern. By increasing the geometry inclination angle, the flow dynamics changes and it is expected that the wear rate will change accordingly. The data above can be replotted to reveal the effect of inclination angle and are given in Figure 6.

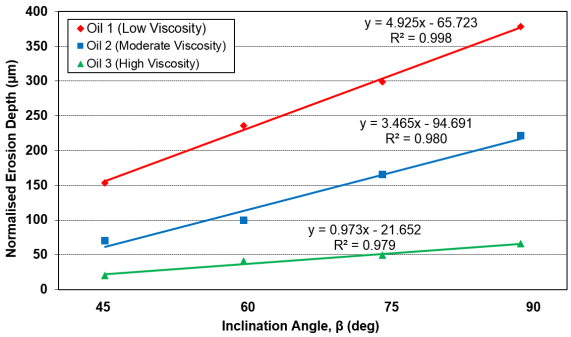

Figure 6: Effect of inclination angle on erosion depth.

A direct linear proportionality exists between the inclination angle and erosion depth. In fact, it can be seen that the effect of the geometrical inclination angle becomes more pronounced as the viscosity of the fluid decreases (or as the effect of the lubricating film decreases) as indicated by the increasing gradient of the regression line.

Effect of Particle Size and Concentration

The particles used for the majority of tests were typical of actual hydro-erosive conditions and consisted of boron carbide micro-grains with a mean size of 4.5 µm. A selected number of tests were rerun with a mean size of 44.5 µm, essentially an order of magnitude size increase to better aid in identifying this effect on the erosion rate. Results are summarised in Figure 7 below.

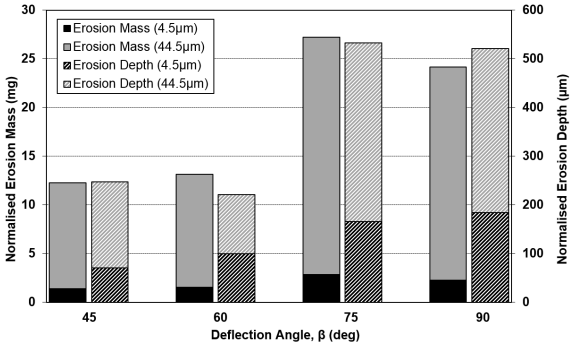

Figure 7: Effect of particle size on erosion mass and depth.

It is clear that the amount of wear has increased markedly with the larger particles size. Interestingly, the increase in erosion mass is approximately equivalent to the ratio of the mean particle sizes, therefore suggesting that a linear correlation with the erosion rate in terms of mass is likely to exist within the range of particle sizes investigated. Also, it is interesting to note that the linear correlation between inclination angle and erosion depth as seen earlier diminishes with larger particles, perhaps suggesting that different particle dynamics, or indeed a combination of impact and abrasion erosion, may be taking place particularly at the higher inclination angles.

Finally, the mass loading of the particles was increased from 1% to 2% in an attempt to quantify the effect of particle concentration on the erosion rate.

The erosion rate did not differ greatly with an increased concentration and only very subtle differences between some of the measured surface contours for low and high levels of concentration could be identified. A possible explanation may be that the concentration was not increased enough to significantly alter the erosion rate or perhaps the maximum packing limit in vicinity of the wall was already reached.

Nevertheless, some of the tests showed a slight but steady increase with increased solids loading. This level of increase could be quantified as φ_p^m, where φ_p denotes the global particle mass fraction and m is the concentration index. A value of $m = 0.7$ was found to best describe the effect of particle concentration and is identical to that obtained by Clark et al., (2000) in their experiments.

COMPUTATIONAL MODEL

CFD Modelling

CFD modelling was used as a tool for establishing the correct flow-field and predicting the subsequent changes in geometry after erosion takes place. The commercial CFD code ANSYS-CFX® was used for the numerical simulations which solves the transport equations as a coupled system using the finite volume method (Eymard et al., 2000). An Eulerian-Eulerian multiphase model was used to represent the slurry flow which involves treating both phases as continuous fluids and solving a set of continuum conservation equations for each phase (Yeoh and Tu, 2009). This approach is seldom used for erosion predictions but was favoured in this case due to its convenience in modelling the abrasion mechanism as a bed of particles sliding along the wall surface. The other advantage is that coupling between the phases is inherent in the formulation of the Eulerian model and is necessary to consider based on the combination of solids fraction and Stokes numbers evident in the present study (Elgohbashi, 1994). Although the overall mass loadings were only 1-2%, the local concentrations predicted near the wall in the numerical simulations were several times higher, therefore warranting the use of two-way coupling.

Inter-particle collisions were not explicitly modelled, although the momentum equations were adjusted to take into account additional solids pressure forces in local areas of high concentration close to the packing limit (Gidaspow, 1994). The equations governing the particle motion consist of various interfacial forces, some of which were neglected for the present study due to their negligible contribution. Besides drag, the forces considered relevant were the virtual mass, Saffman lift and turbulent dispersion forces. Whilst it can be argued that the 'drift-flux' model could have been used for the present study, the main reasons are documented in Rizkalla, (2007) but relate to the fact that the solids pressure and interfacial forces described above could not be considered.

A second order backward Euler scheme was used for the advection and transient terms and first order (upwind) for turbulence. Turbulence was modelled using the RANS-based SST model (Menter, 1994). This was chosen as it was important to accurately capture the effect of the boundary layer, including the viscous sublayer which was expected to govern the particle dynamics close to the wall given the small Stokes numbers involved, which varied between 0.01 to 0.1 for the highest and lowest fluid viscosities, respectively. A parametric model of the geometry and mesh for one of the configurations is shown below.

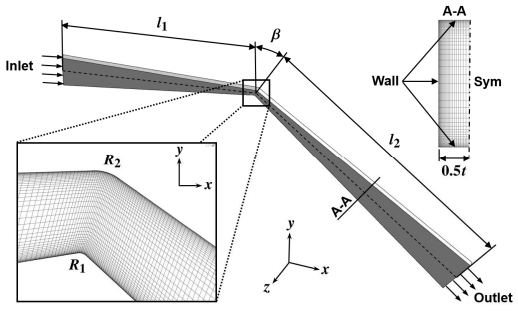

Figure 8: Parametric model of the geometry and mesh.

The mesh was created using ANSYS ICEM CFD® and consisted of approx. 275,000 hexahedral elements (for a symmetric model) having a minimum orthogonality and maximum skewness of 0.35 and 0.55, respectively. The 'near-wall' mesh was sufficiently refined ($y^+ < 1$) to ensure the boundary layer effect on the particle-wall interaction was accurately modelled (see Figure 8). A mesh displacement diffusion scheme was used to simulate the material removal process with a high stiffness used near the wall to preserve the boundary layer mesh during deformation.

Abrasion Model Formulation

There have been a number of pioneers in the field of erosion modelling including Finnie (1960), Bitter (1963), Grant and Tabakoff (1975), Magnêe (1995) and others. Their *impact* models essentially relate the erosion rate to the particle velocity, mass, impingement angle and some empirical constants that describe the material properties and in some cases the effect of particle shape. The fundamental difference in this study is that the proposed model is based on shear work and predicts maximum erosion at zero impingement angle as the particle slides along the wall surface. This type of erosion is more commonly known as *abrasion* and takes place when the particle does not impact and rebound over a short time, rather, it becomes trapped within the viscous layer adjacent to the wall and slides for a relatively long period of time. This means that the mechanism of energy transfer (i.e. change in kinetic energy) between the particle and wall is no longer due to rapid momentum exchange, rather, it is the work energy imparted by the fluid on the particles as they slide along the wall. The proposed abrasion model consists of a tangential and normal component. Figure 9 shows the various forces and velocities used in the model formulation.

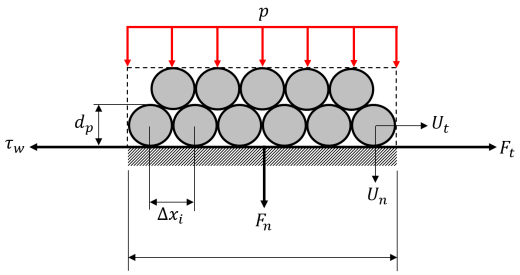

Figure 9: Free body diagram showing relevant forces during abrasion.

Tangential Component

The tangential component can be derived using work energy principles,

$$W_e = \Delta E_k = \int F_t(t)\, dx_i \qquad (1)$$

where, x_i represents the distance travelled by the particle in the i-th direction and $F_t(t)$ the tangential fluid force exerted on the particle. This force can be taken to be the magnitude of the wall shear stress, τ_w and is assumed constant as the particle migrates along the wall within a time step. In light of this, the time step, Δt, should be chosen based on the local Courant number such that the sliding length of the particle does not exceed the length of the cell in which it slides, (i.e. $l_{\text{cell}} > U_t\, \Delta t$). This yields a maximum allowable time step of $\Delta t = l_{\text{cell}}\,/U_t$ and the work done within a single time step may be simplified to,

$$W_e = \sum_{l} F_t\, \Delta x_i \qquad (2)$$

By defining the total sliding distance travelled by all particles within a control volume as

$$l_s = \sum_l \Delta x_i = U_t t \tag{3}$$

Substitution into equation (2) yields the tangential component of energy transfer responsible for abrasive wear.

$$W_e = \Delta E_K = \tau_w A_w . U_t t \tag{4}$$

By taking into account the fluid viscosity, particle size and concentration effects observed from the experiments, and noting that $U_t = U_p \cos\alpha_p$, equation (4) can be conveniently expressed as volume of material removed (per unit area)

$$W_t = \frac{C_a . Re_p . \varphi_p^m . \tau_w}{\gamma_c} . U_p \cos(\alpha_p)\, t, \quad \tau_w > 0 \tag{5}$$

where $C_a = k_a \lambda_p$ is a dimensionless abrasion constant that is a combination of the abrasion amplitude, k_a and particle shape factor, λ_p as defined by Krushchov and Babichev, (1964) and Magnêe, (1993), respectively. A full derivation is contained in Rizkalla, (2007).

Normal Component

The normal component of abrasive wear can be derived using Archard's law (Archard, 1953) which relates the degree of wear to the normal force component.

$$W_n = \frac{k_a}{3} \frac{F_n . l_s}{H_w} \tag{6}$$

This component of abrasion can have a significant contribution in regions of high pressure gradient (i.e. at elbow bends, pipe intersections, etc.) as the bed of particles presses against and slides along the wall. By taking the normal force as the product of the pressure gradient and representative particle volume, the normal component of abrasive wear can be expressed as

$$W_n = -\frac{1}{3} \frac{C_a}{H_w} \frac{\partial p}{\partial n} \frac{m_p}{\rho_p} U_p \cos(\alpha_p)\, t, \qquad \frac{\partial p}{\partial n} < 0 \tag{7}$$

Statistical Modelling of Particle Impact Angle and Mass

Unlike the Lagrangian framework where the impact mass and angle are readily available for each particle, the choice of an Eulerian approach to model the dispersed phase meant that a statistical model was necessary to define the particle impact-angle, velocity and mass flux, since only averaged values within the 'near-wall' cell are available. The instantaneous velocity was calculated by summing the mean and fluctuating velocity components, $U_p = \overline{U}_p + U'_p$. The mean component can be estimated by relating the particle velocity to the wall shear stress via the relationship

$$\tau_w = \mu \left(\frac{\partial \overline{U}_p}{\partial \eta} \right) \Bigg|_{\eta = r_p} \tag{8}$$

and the fluid viscosity was adjusted according to particle concentration via Eilers-Chong relationship (Kissa, 1999)

$$\mu = \mu_f \left[1 + \frac{1.25 \phi_p}{1 - \phi_p / \phi_{cr}} \right] \tag{9}$$

where ϕ_{cr} is the critical volume fraction for maximum packing taken to be 0.64 for random packing of spherical particles. This method of estimating the particle velocity reduces the mesh dependency near the wall but is only valid when the Stokes number is sufficiently small and the particle size does not exceed the boundary layer thickness, both which were fulfilled in the present study.

The fluctuating component, U'_p was modelled statistically using a Probability Density Function (PDF). The PDF of the fluctuating velocity component, $f(U_p)$, has a Gaussian distribution with standard deviation, $\sigma = \sqrt{2k/3}$, assuming isotropic normal stresses, as shown in Figure 10.

$$f(U_p) = \frac{1}{\sigma\sqrt{2\pi}} . e^{-\frac{1}{2}\left(\frac{U_p - \zeta}{\sigma}\right)^2} \tag{10}$$

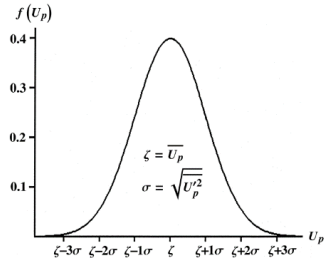

Figure 10: Probability density function of the instantaneous velocity component, U_p.

Integration of the PDF yields the probability that a given mass of particles will possess a given velocity

$$P(U_i < U_p \leq U_i + \Delta U_p) = \frac{1}{\sigma\sqrt{2\pi}} . \int_{U_i}^{U_i + \Delta U_p} e^{-\frac{1}{2}\left(\frac{U_p - \zeta}{\sigma}\right)^2} dU_p \tag{11}$$

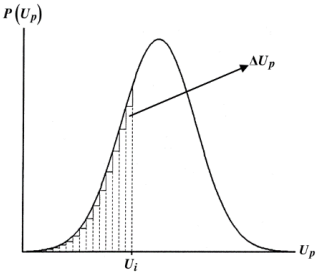

Figure 11: Integration of the probability density function.

Since the SST turbulence model assumes an isotropic eddy viscosity, the distributions for the remaining velocity components will have the same standard deviation but will differ in their mean value. As shown in Figure 11, the particle velocity can be discretised and split into different mass groups of identical particles, where the probability that each group having a certain velocity is represented by the area under the integration function with width ΔU_p. It follows that the probability and velocity magnitude in three-dimensions can be evaluated as

$$P_{ijk} = P\left[(U_1)_i \cap (U_2)_j \cap (U_3)_k \right] \tag{12}$$

$$(U_p)_{ijk} = \sqrt{(U_1)_i^2 + (U_2)_j^2 + (U_3)_k^2} \tag{13}$$

Therefore, the mass flux of particles, together with their corresponding impact angle, for a given combination of classes ijk, in three-dimensional form can be expressed as

$$(m_p)_{ijk} = P_{ijk} . \Delta V \phi_p . \rho_p \ \text{ for } (\alpha_p)_{ijk} \geq 0 \tag{14}$$

$$(\alpha_p)_{ijk} = \sin^{-1} \left(\frac{(U_p)_{ijk} . \vec{n}}{\left| (U_p)_{ijk} \right|} \right) \tag{15}$$

In the case where a negative impact angle results, impact erosion does not take place and indicates that the particles are being moved away from the wall. These particles may however, still be responsible for abrasion if they possess energy which is high enough to cause significant wear but not enough to penetrate the thin squeeze film and are therefore unable to escape from the wall (i.e. they remain trapped within the squeeze film). This criterion is assessed by comparing the normal Reynolds number of the particle with a critical Reynolds number required for particle-wall contact as suggested by Clark and Burmeister, (1992).

$$Re_{cr} = \frac{12\xi^2}{a^*} \tag{16}$$

where, $a^* = 8\left[1 + 2\left(\rho_p/\rho_f\right)\right]$ and $\xi = 10$.

When contact does occur, the effect of the squeeze film reduces the particle's normal velocity component, U_n, by a factor F given by

$$F = \frac{a^*}{a^* + \xi} - 12\frac{\xi^2}{a^* + \xi}\frac{1}{Re_n} \tag{17}$$

Implementation of Erosion Model in ANSYS CFX®

Implementation of the proposed model was accomplished via a user Fortran subroutine which calls the erosion function at each time step. The total erosion quantity is the sum of the impact and abrasive contributions (either or both can be present) and this is normalised with respect to the cell face area such that a displacement value is calculated and used to automatically update the mesh via the in-built mesh morphing algorithm available in ANSYS CFX®. A simplified flowchart outlining the program algorithm is shown in Figure 12.

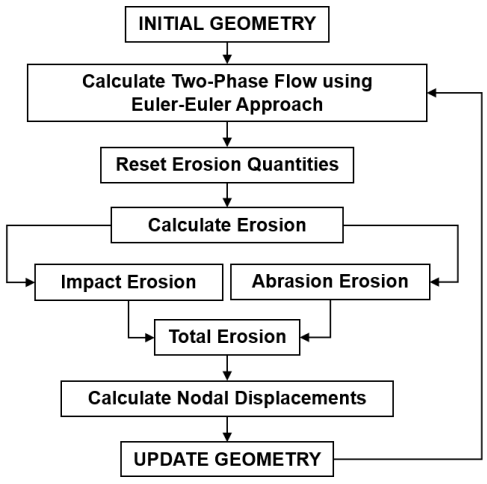

Figure 12: Basic outline of program structure.

A steady-state solution of the flow-field in the original undeformed geometry was solved initially without activating the erosion model. This allowed the slurry flow to fully develop and provided an initialisation for the transient solution with erosion. Since the erosion timescales are much larger than that of the fluid, the quantities were extrapolated assuming a linear erosion rate within each erosion time step. A fluid time step of 10^{-5} seconds was used and extrapolated linearly per second of erosion time. The solution was considered converged when RMS residual values dropped below 1.0^{-4} or when 5 iterations per time step was reached.

RESULTS AND DISCUSSION

Model Calibration

In order for the numerical model to be capable of quantitatively predicting meaningful values of wear, the empirical values were required to be calibrated or adjusted such that a single set of universal values would deliver correct erosion quantities independent of the system parameters. According to Khruschov, (1964) abrasion amplitude values ranging between 10^{-1} to 10^{-8} have commonly been used depending on the wear conditions being defined as either heavy or moderate, respectively. Since not enough information on the particle shape was available, the particle shape factor was set to unity and the value for the abrasion amplitude was gradually increased until the desired rate of wear were obtained. The values for specific cutting energy and wall hardness are characteristic properties of the erosion specimen, however some fine-tuning was still necessary to obtain the appropriate values for the stainless steel material used in this study. A summary of the empirical constants used for the present study are given below in Table 2.

Abrasion Amplitude	Particle Shape Factor	Specific Cutting Energy (J m^{-3})	Wall Hardness (N m^{-2})
10^{-5}	1.0	26×10^9	2.52×10^9

Table 2: Empirical constants used in the numerical model.

Numerical Validation and Comparison with Experiments

In order to assess the accuracy of the proposed model, the experimentally measured erosion lengths and depths were compared with those predicted numerically. A centreline plot and surface contour for one of the numerically predicted erosion profiles is shown in Figure 13 and a comparison between the measured and predicted erosion quantities for tests 1-15 are shown in Figure 14.

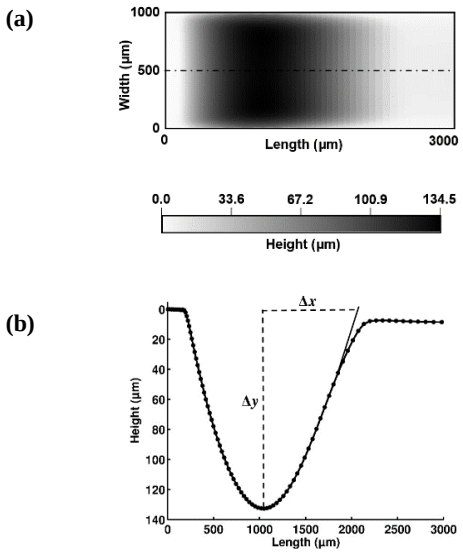

Figure 13: Erosion contour map predicted for a selected sample using CFD simulation (a) surface plot and (b) centreline profile.

Overall, the numerical results are in close agreement with the experimentally measured surface profiles. In fact, the maximum error was <20% across all tests. The average error for the erosion length predictions were generally

greater than those for the erosion depths since it was more difficult to quantify this experimentally and in some cases, the precise location of erosion (i.e. point of commencement and termination) could not be easily identified.

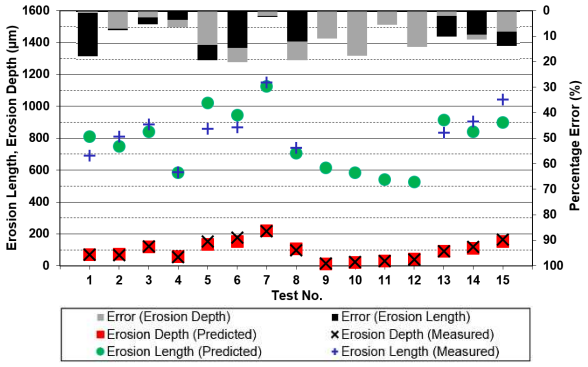

Figure 14: Comparison of experimentally measured and numerically predicted erosion quantities.

An interesting phenomena that was qualitatively observed in the experiments and captured in the simulations, was the presence of an area of high localised wear intensity on the lower surface just after the bend and close to the edges as shown below in Figure 15.

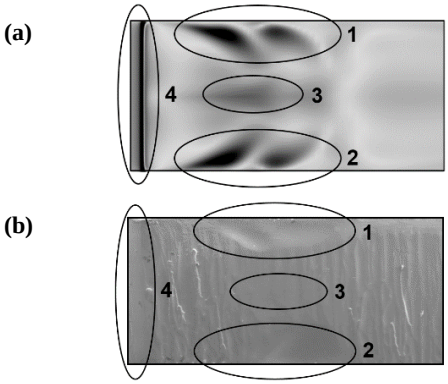

Figure 15: Contour plot of the wall shear stress from a steady-state simulation (a) and SEM exposure of the same surface (b).

This erosion pattern was consistent on almost every test specimen. The simulation results reveal the formation of two counter-rotating vortices (Dean vortices) arising from secondary flow on the low pressure side of the bend at this precise location, indicated by zones 1 and 2. It can be seen that very light surface smoothing has taken place at zone 3 and more aggressively at zone 4.

This comparison confirms that the shear stress indeed plays a significant role in the abrasive wear process and that single-phase steady-state simulations can still be employed in order to estimate the location of abrasive wear. However, a precise prediction of the quantity of material removal, particularly for larger deformations and changes in geometry, can only be accomplished by means of a transient simulation which updates the flow field iteratively.

Despite the good agreement between experimentally measured and numerically predicted results, there are some differences evident, most likely due to underlying assumptions and model simplifications. Since the numerical model assumes perfectly symmetrical conditions and an infinitely smooth wall, it fails to predict the asymmetrical profiles which were typical of the physical tests and are likely to be caused by surface imperfections, geometry manufacturing tolerances, particle shape variability and wall roughness.

Wall roughness was not accounted for in the simulations as it was assumed its effect on the particle-wall contact and impingement angle would only be significant in the initial stages of the wear process, but still overall negligible. This is only true however for large erosion depths as was seen in the case of low to moderate fluid viscosities, where the roughness height was considered relatively small in comparison to the final erosion depth. In the case of the highest viscosity oil however, the erosion depth was of the same order of magnitude as the roughness height, suggesting that wall roughness was dominant in governing the particle-wall interaction and cannot be ignored. In such cases, it may be necessary to implement a wall roughness model such as that proposed by Sommerfeld, (1992). This possibly explains the vast difference in erosion profiles for these tests and variation in the measured erosion lengths.

CONCLUSION

A new erosion model was developed which describes the abrasion mechanism, found to be the dominant component of wear in the present study. This model has been added to the commercial CFD code ANSYS CFX®, and takes into account transient changes in geometry by displacing the mesh proportional to the erosion rate. An Eulerian approach was used to model both fluid and particulate phases as it was considered to be more practical in terms of the abrasion model implementation.

The model was validated against experimental measurements using simplified geometries to understand the effect of geometry inclination angle, fluid viscosity, particle size and concentration. These findings were used as a basis for the developed model which yielded erosion lengths and depths that were consistent with experimental observations. Furthermore, it is expected that a similar degree of accuracy be reproduced when applied to more complex systems placed under similar erosive conditions.

ACKNOWLEDGMENTS

The author would like to thank the research and development teams at Robert Bosch Pty Ltd in Bamberg and Stuttgart, Germany for their exceptional support and use of their test facilities during the course of this work.

REFERENCES

ARCHARD, J. F., (1953), “Contact and rubbing of flat surfaces”, *J. Appl. Phys.*, **24**, 981–988.

BITTER, J.G.A. (1963), "A study of erosion phenomena: (Parts 1 and 2)”, *Wear*, **6**, 5-21 & 169-190.

CLARK, H. McI. and BURMEISTER, L. C., (1992), “The influence of the squeeze film on particle impact velocities in erosion”, *Int. J. of Impact Eng.*, **12**, 415–426.

CLARK, H. McI., TUZSON, J., and WONG, K., (2000), “Measurements of specific energies for erosive wear using a Coriolis erosion tester”, *Wear*, **241**, 1–9.

ELGHOBASHI, S. E, 1994 “On predicting particle-laden turbulent flows”, *Appl. Sci. Res.*, **52**, 309–329.

EYMARD, R., GALLOUET, T., and HERBIN, R., (2000), “Finite volume methods”, *Handbook of numerical analysis*, Vol. **VII**, 713–1020. North-Holland, Amsterdam,

FINNIE, I. (1960), "Erosion of surfaces by solid particles", *Wear*, **3**, 87-103.

GIDASPOW, D., (1994), "Multiphase flow and fluidisation", *Academic Press*, London

KISSA, E., (1999), "Dispersion: Characterisation, Testing and Measurement", Vol. **84**, Marcel Dekker Inc.

KHRUSCHOV, M. M and BABICHEV, M. A., (1964), "Experimental fundamentals of abrasive wear theory", *Russian Eng. J.*, Vol. **44**, 43-47.

MAGNÊE, A., (1993), "Modelisation of damage by abrasion", *Wear*, **162-164**, 848-855.

MAGNÊE, A., (1995), "Generalised law of erosion: Application to various alloys and intermetallics", *Wear*, **181-183**, 500–510.

MENTER, F. R., (1994), "Two-equation eddy-viscosity turbulence models for engineering applications", *AIAA J.*, **32**, 1598–1605, 1994.

RIZKALLA, P., (2007), "Development of a Hydro-erosion Model using a Semi-Empirical Method Coupled with an Euler- Euler Approach", *Doctoral Thesis*, Royal Melbourne Institute of Technology, VIC Australia.

SOMMERFLD, M., (1992), "Modelling of particle wall collisions in confined gas-particle flows", *Int. J. Multiphase Flow*, **18**, 905–926.

TABAKOFF, W. and GRANT, G., (1975), "Erosion prediction in turbomachinery resulting from environmental solid particles", *J. Aircraft*, **12**, 471–478.

YEOH, G.H. and TU, J., (2009), "Computational techniques for multiphase flows", Butterworth-Heinemann, Elsevier, UK.

